Supporting Information for

Ferroionic Heterostructures with Reconfigurable Free-energy Surface and Band Alignment across CuInP2S6 van der Waals Interface with Boron Nitride and Graphene

Hejin Yan[a†], Bowen Wang[a†], Gian-Marco Rignanese[b], Yongqing Cai[a*]

[a]Institute of Applied Physics and Materials Engineering, University of Macau, Taipa, Macau, 999078, China

[b]Institute of Condensed Matter and Nanosciences, UCLouvain, Louvain-la-Neuve, 1348, Belgium

[*]**Corresponding Author**

[†]**Contribute equally**

Yongqing Cai* E-mail: yongqingcai@um.edu.mo

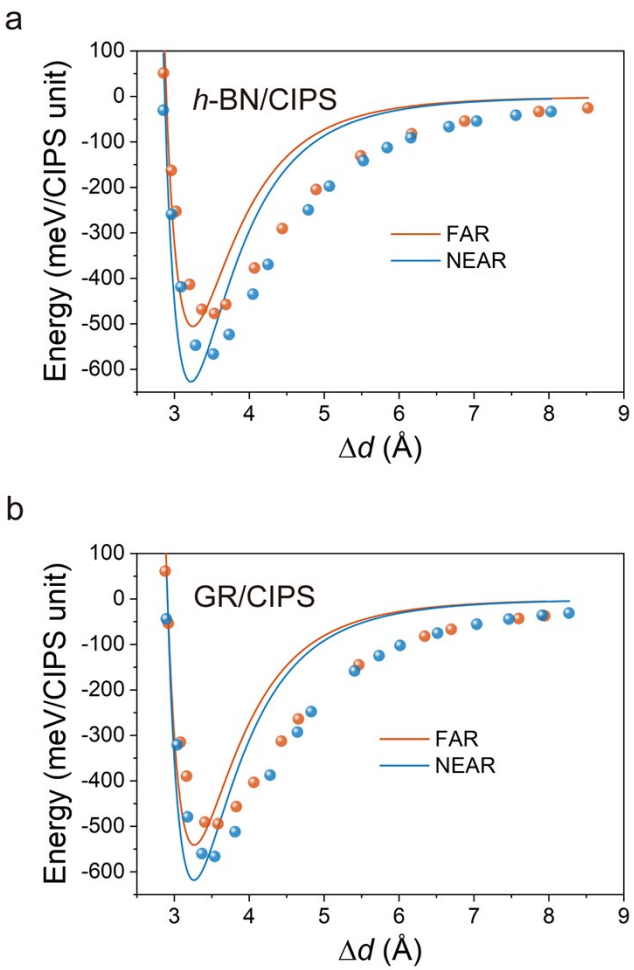

Figure S1. Fitted Lennard-Jones (LJ) potential of the (**a**) *h*-BN/CIPS and (**b**) GR/CIPS heterostructures. The discrete solid circles denote energy values obtained from DFT calculations, and the solid lines represent fitted energy curves based on the LJ potential.

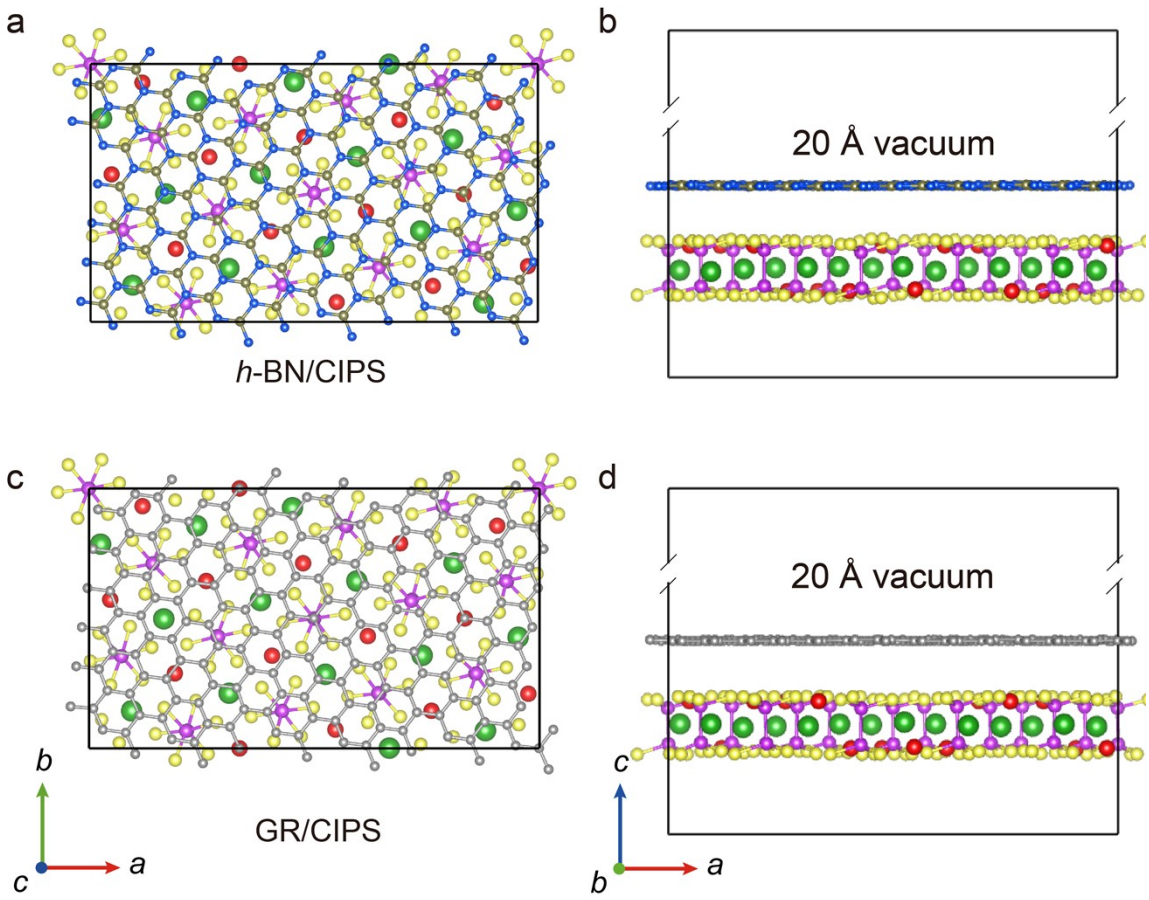

Figure S2. (**a, b**) Top and side views of *h*-BN/CIPS at PARA state. (**c, d**) Top and side views of GR/CIPS in the PARA state.

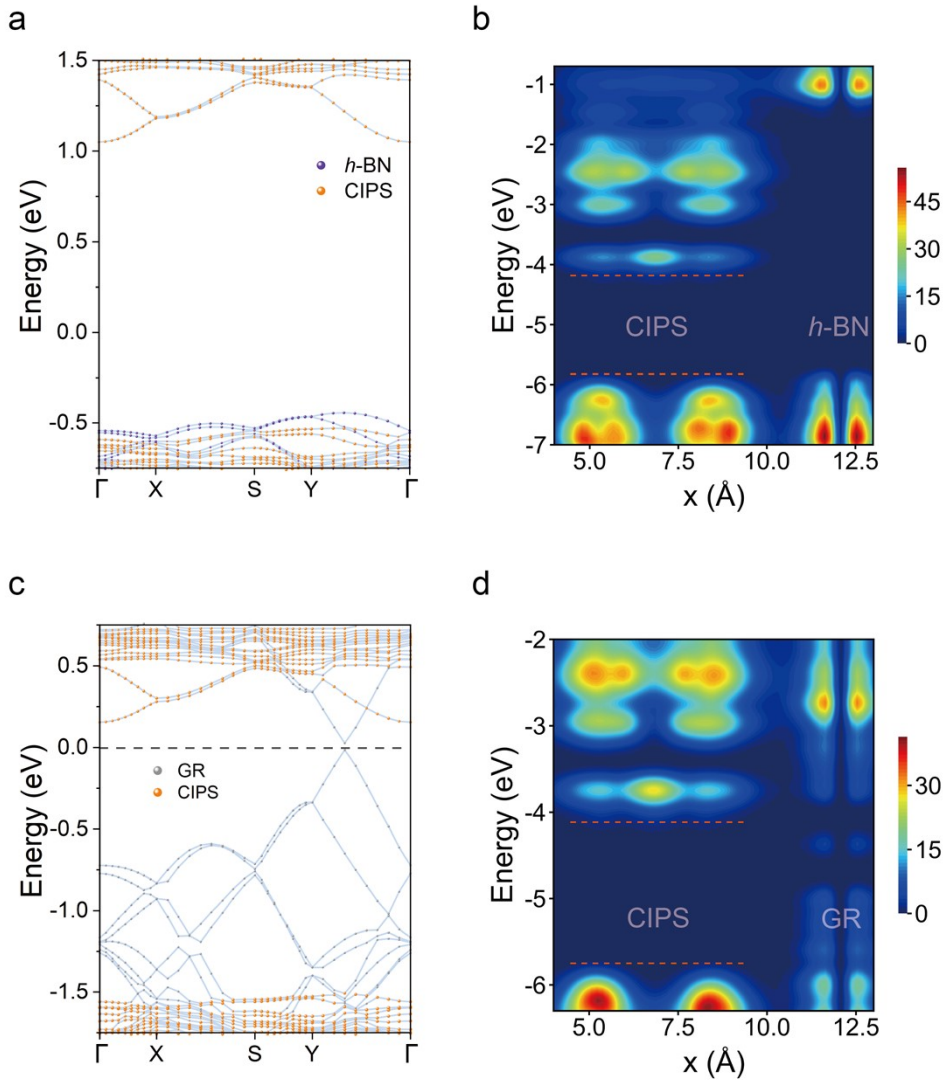

Figure S3. (**a**) Band structure and (**b**) LDOS of *h*-BN/CIPS in the PARA state. (**c**) Band structure and (**d**) LDOS of GR/CIPS in PARA state. On the left side, solid circles represent contributions from certain slabs, and the dashed line denotes the Fermi level position. On the right side, dashed orange lines guide the eye to band edge tilting within the CIPS layer.

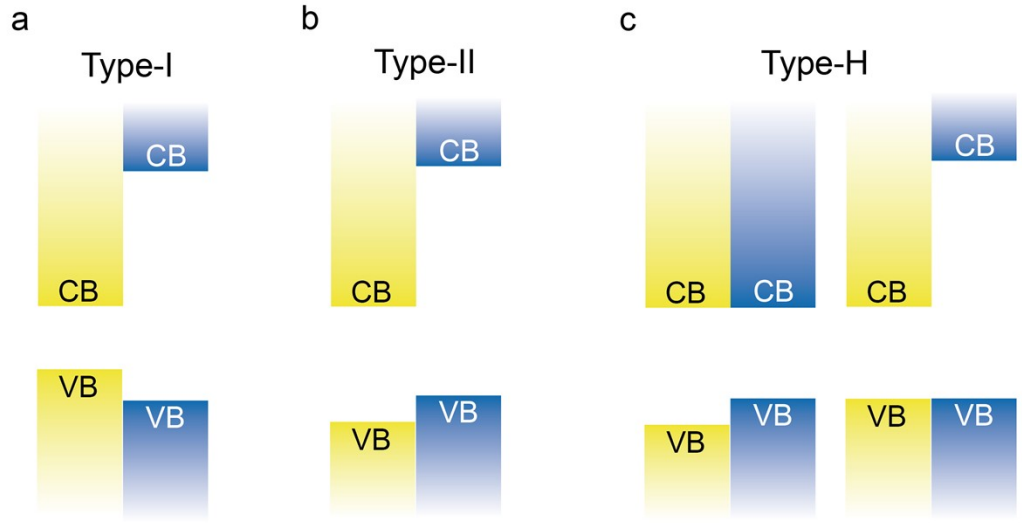

Figure S4. Schematic illustration of band alignments for heterostructures, including (**a**) type-I, (**b**) type-II, and (**c**) type-H alignments.

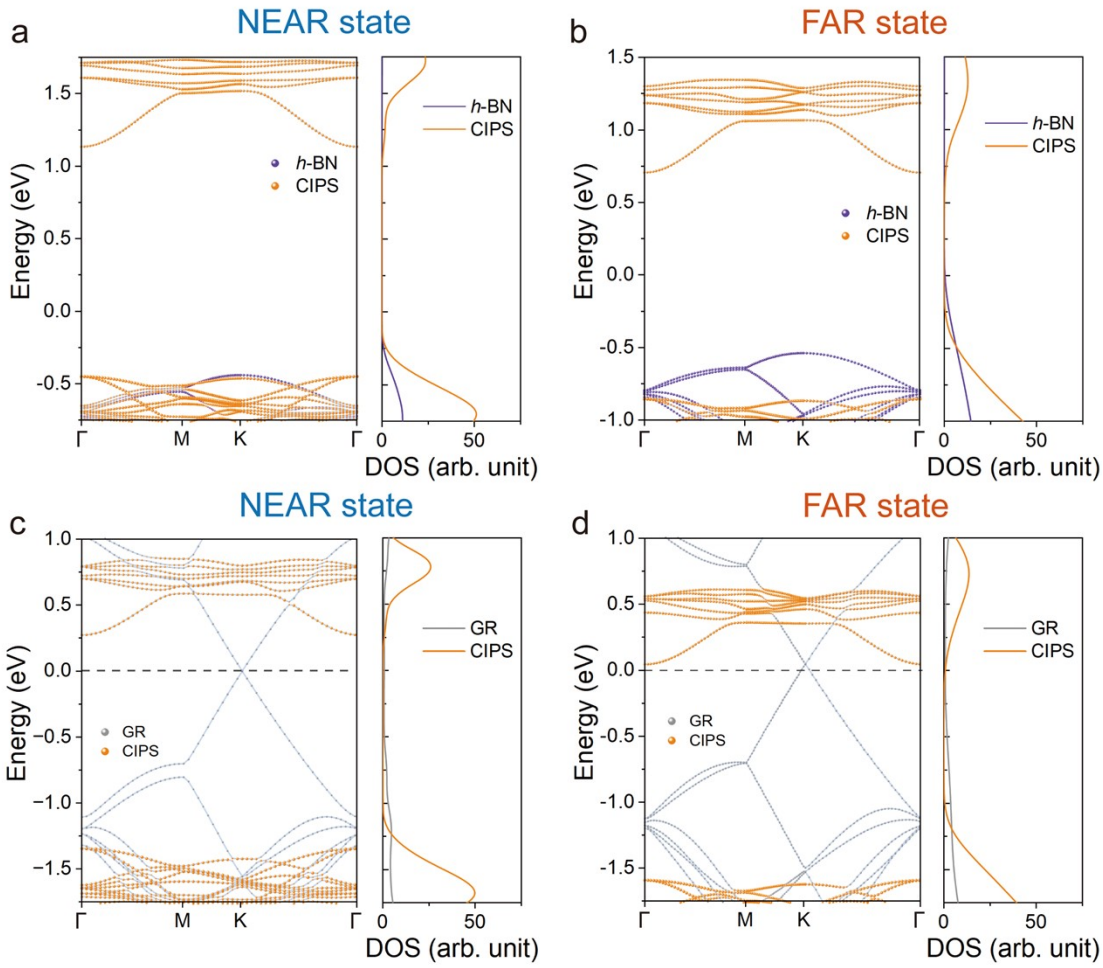

Figure S5. Electronic structures of vdW *h*-BN/CIPS and GR/CIPS heterostructures depending on the polarized state in CIPS. Band structures and density of states (DOS) of *h*-BN/CIPS in (**a**) NEAR and (**b**) FAR states and GR/CIPS in (**c**) NEAR and (**d**) FAR states. The left panels show projected band structures, and the right panels show the corresponding projected DOS. The Fermi level is set to zero and indicated by dashed lines.

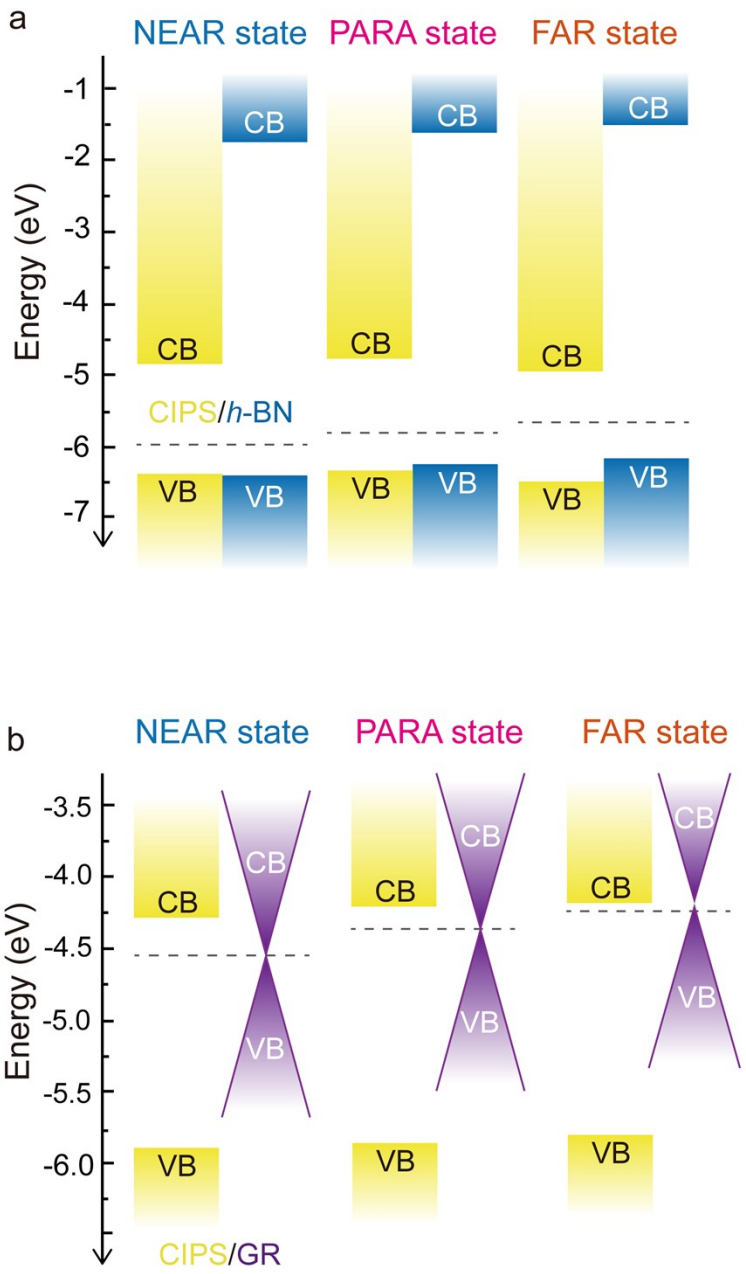

Figure S6. Band alignments of (**a**) *h*-BN/CIPS and (**b**) GR/CIPS at three different states.

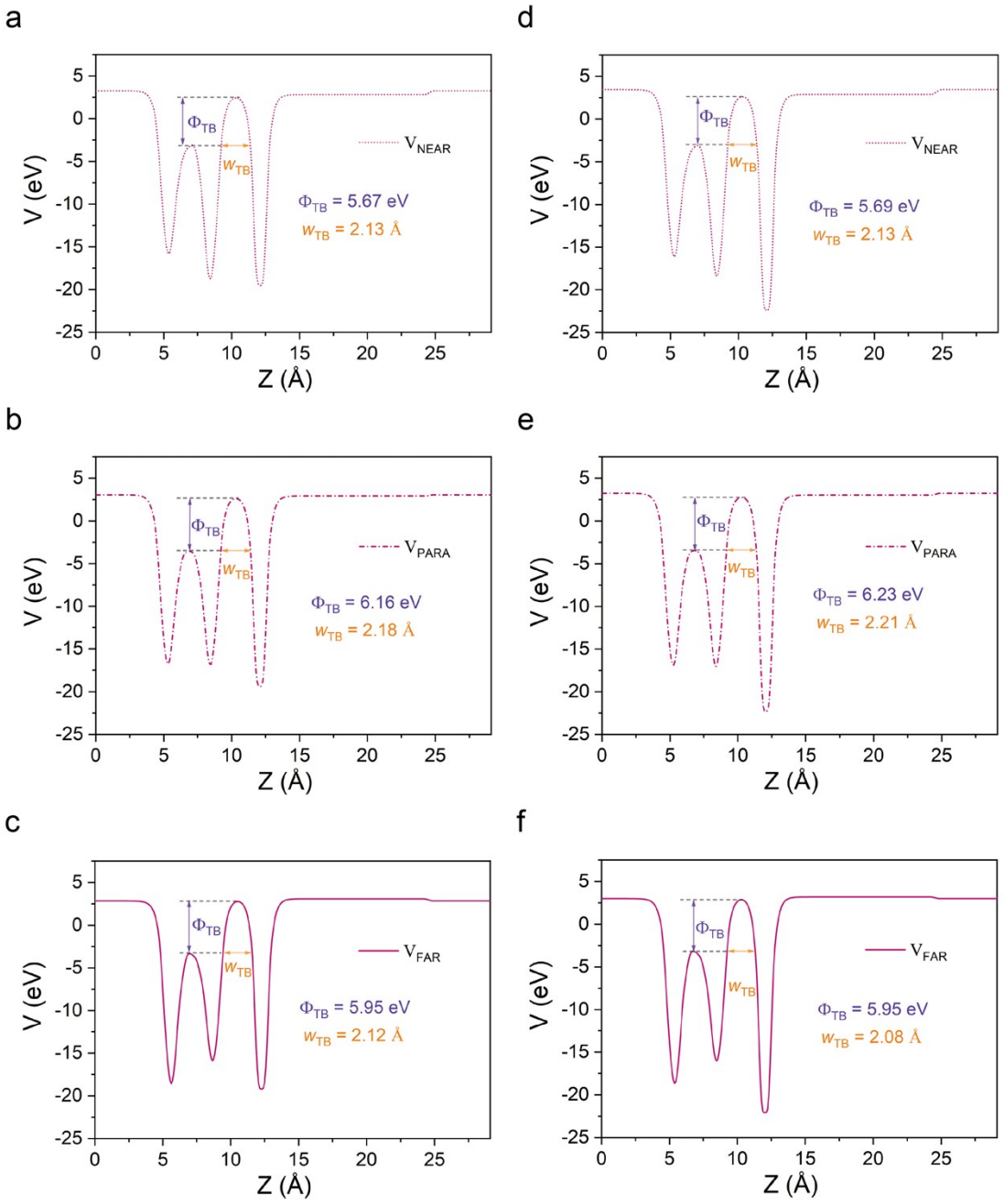

Figure S7. Planar-averaged electrostatic potential of (**a-c**) *h*-BN/CIPS and (**d-f**) GR/CIPS at three different states. The w_{TB} and Φ_{TB} are the width and height of the tunneling barrier.

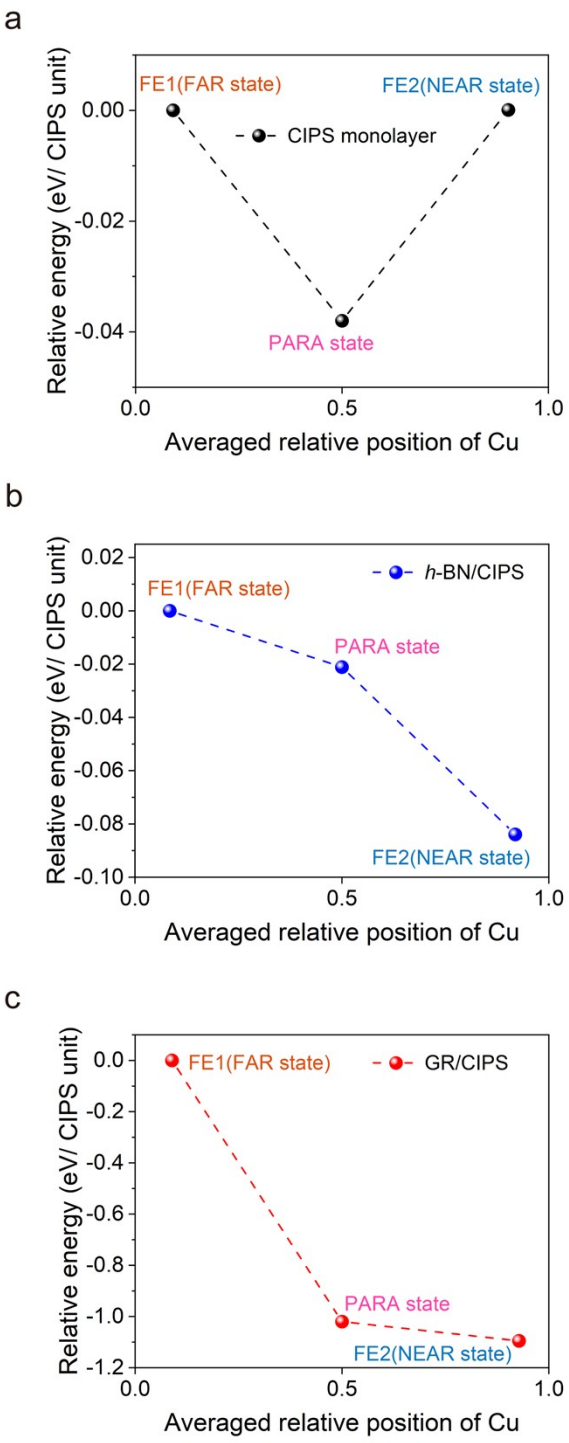

Figure S8 Comparison of energy of (**a**) CIPS monolayer and (**b**) *h*-BN/CIPS and (**c**) GR/CIPS heterostructures in different polarization states.

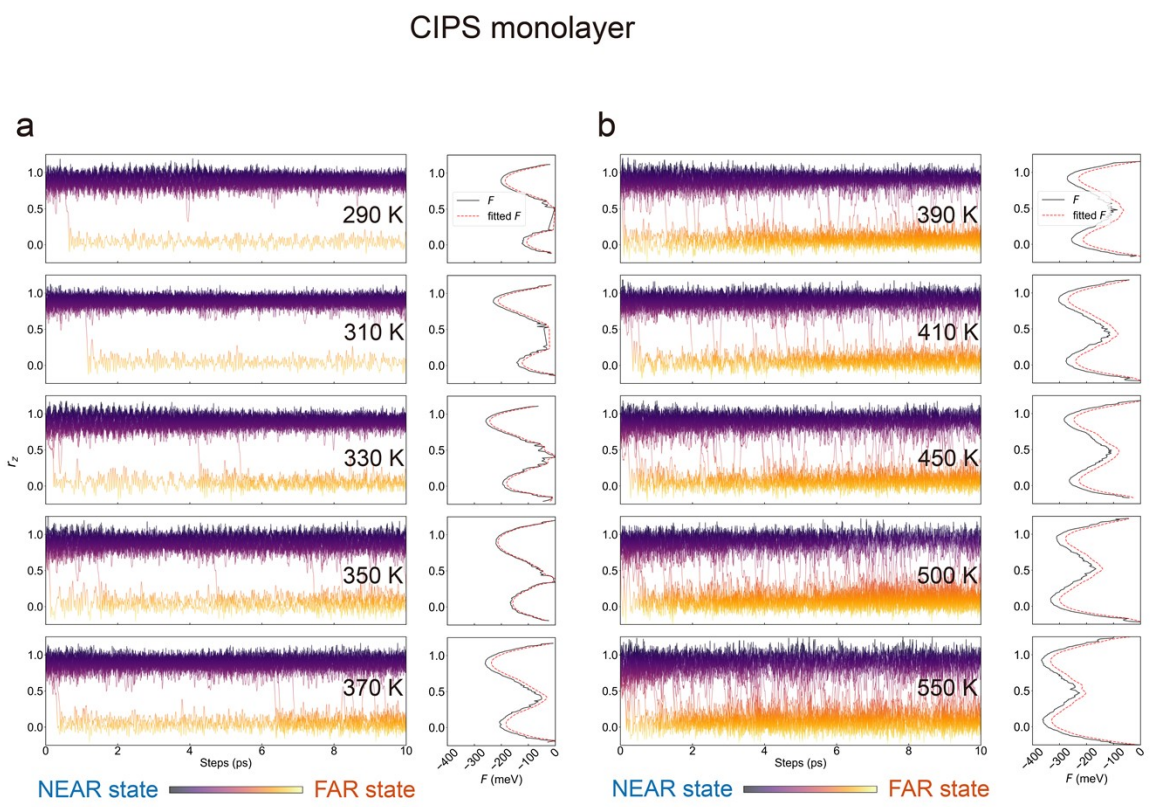

Figure S9. Temperature-dependent state switching dynamics and barriers in the CIPS monolayer. The upper state is selected as the initial state.

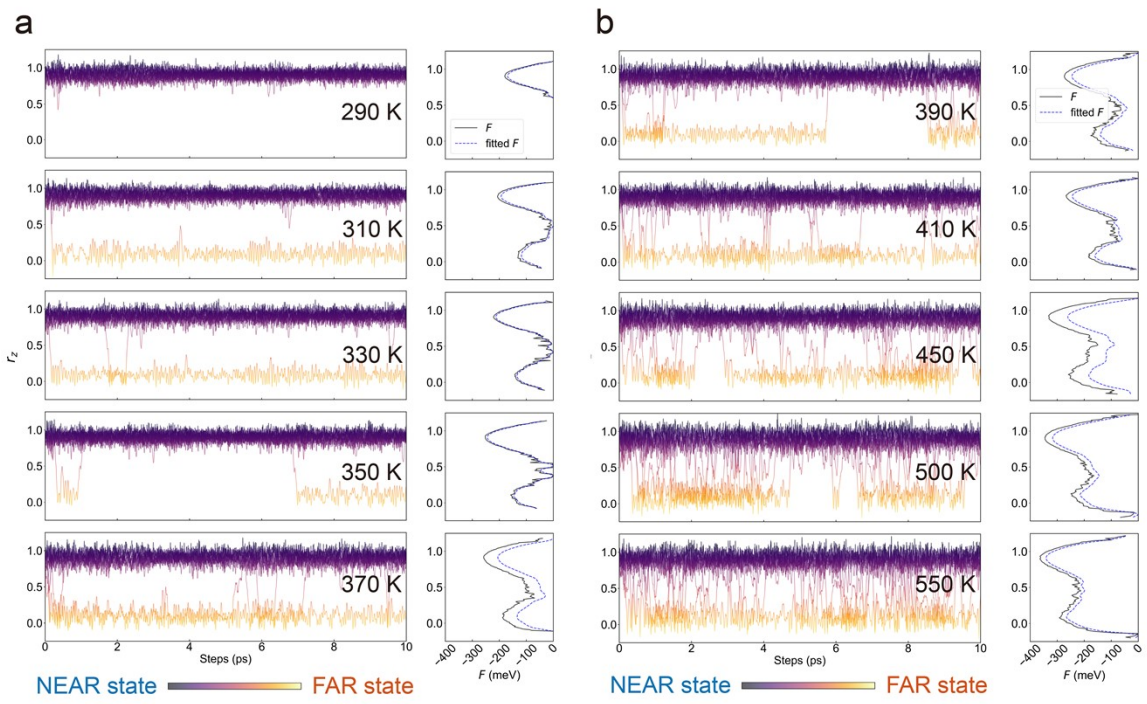

Figure S10. Temperature-dependent state switching dynamics and barriers in *h*-BN/CIPS heterostructure. The NEAR state is selected as the initial state.

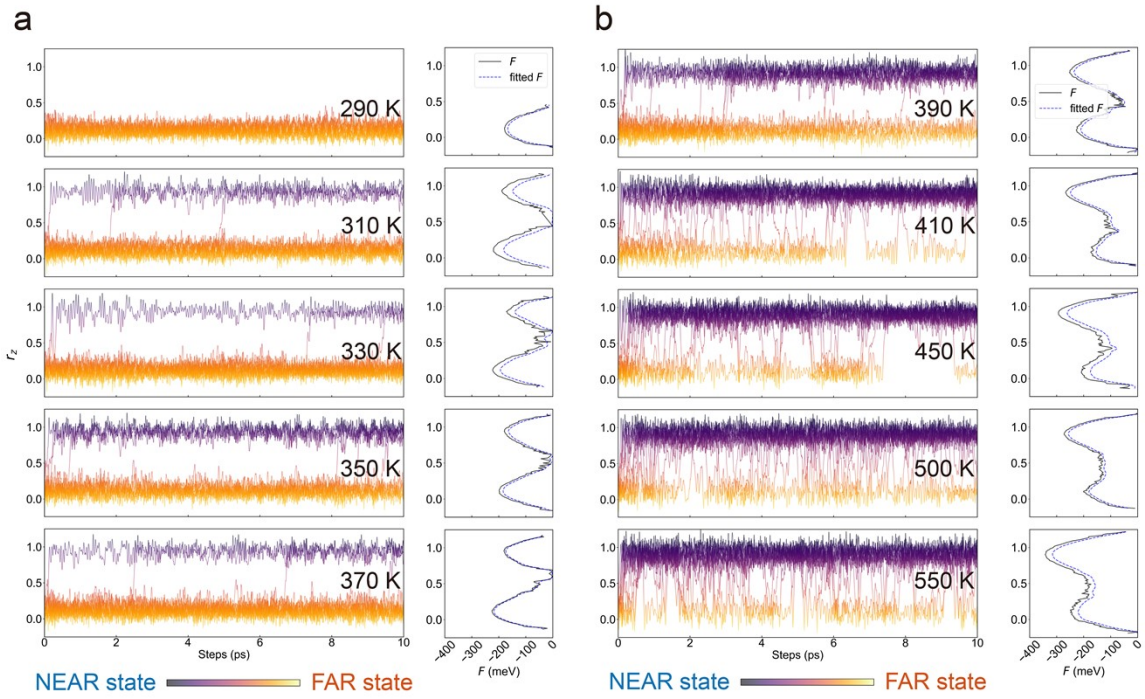

Figure S11. Temperature-dependent state switching dynamics and barriers in *h*-BN/CIPS heterostructure. The FAR state is selected as the initial state.

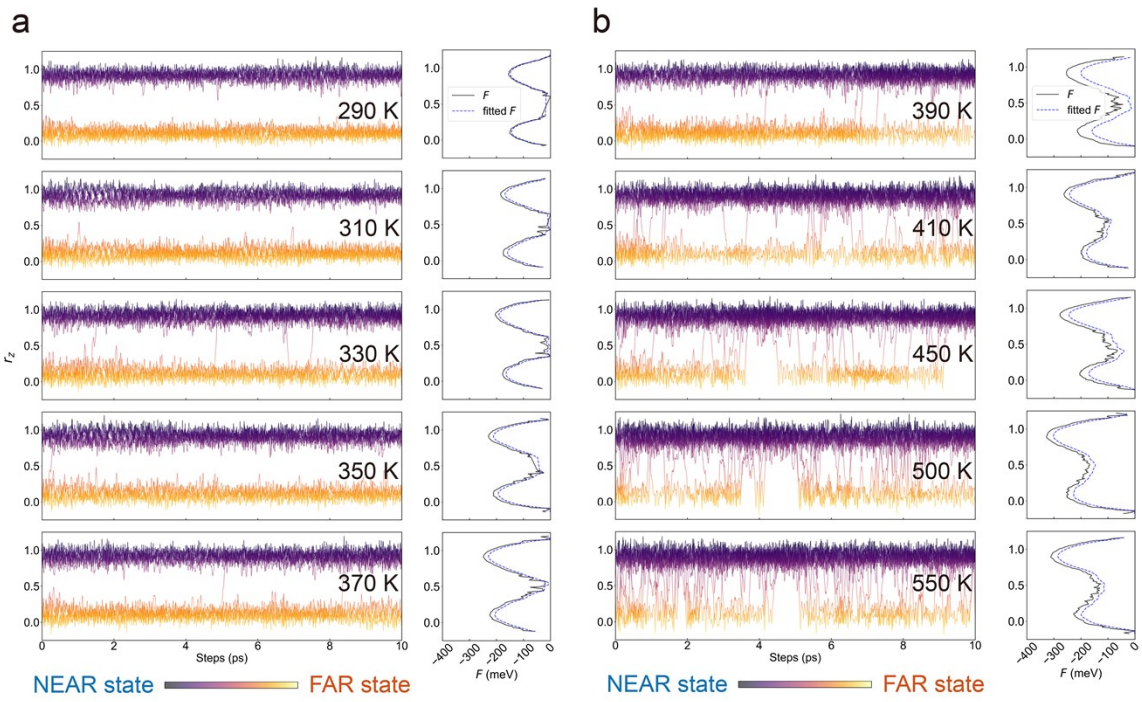

Figure S12. Temperature-dependent state switching dynamics and barriers in *h*-BN/CIPS heterostructure. The PARA state is selected as the initial state.

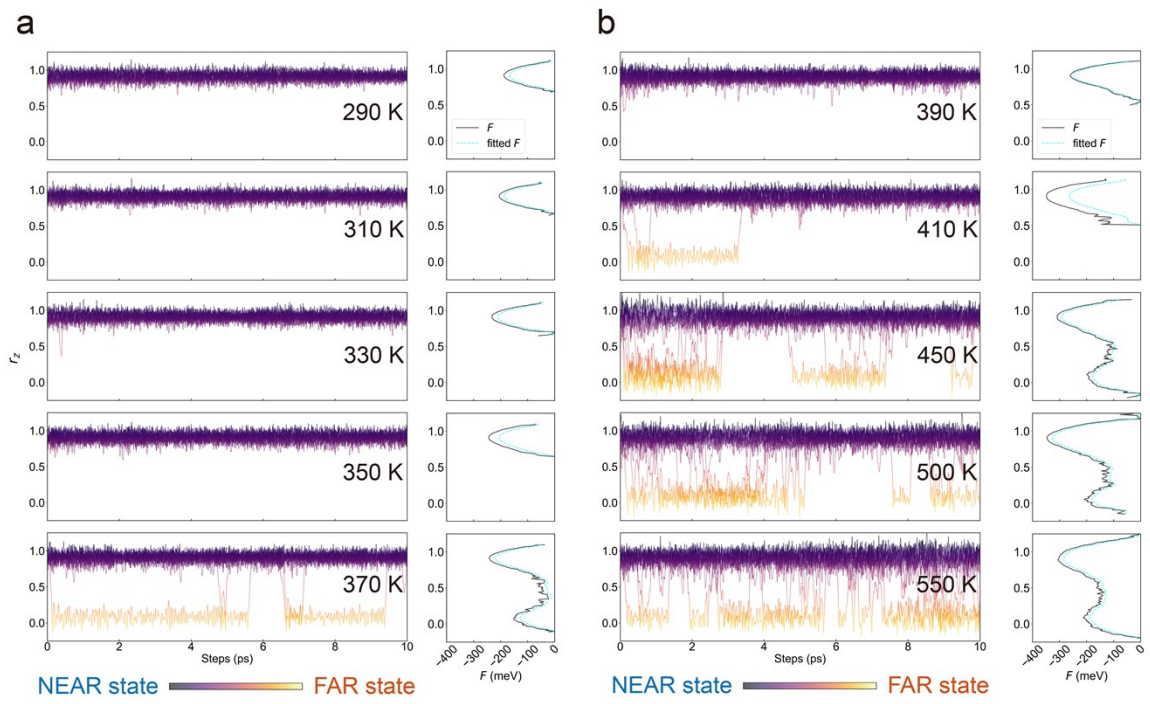

Figure S13. Temperature-dependent state switching dynamics and barriers in GR/CIPS heterostructure. The NEAR state is selected as the initial state.

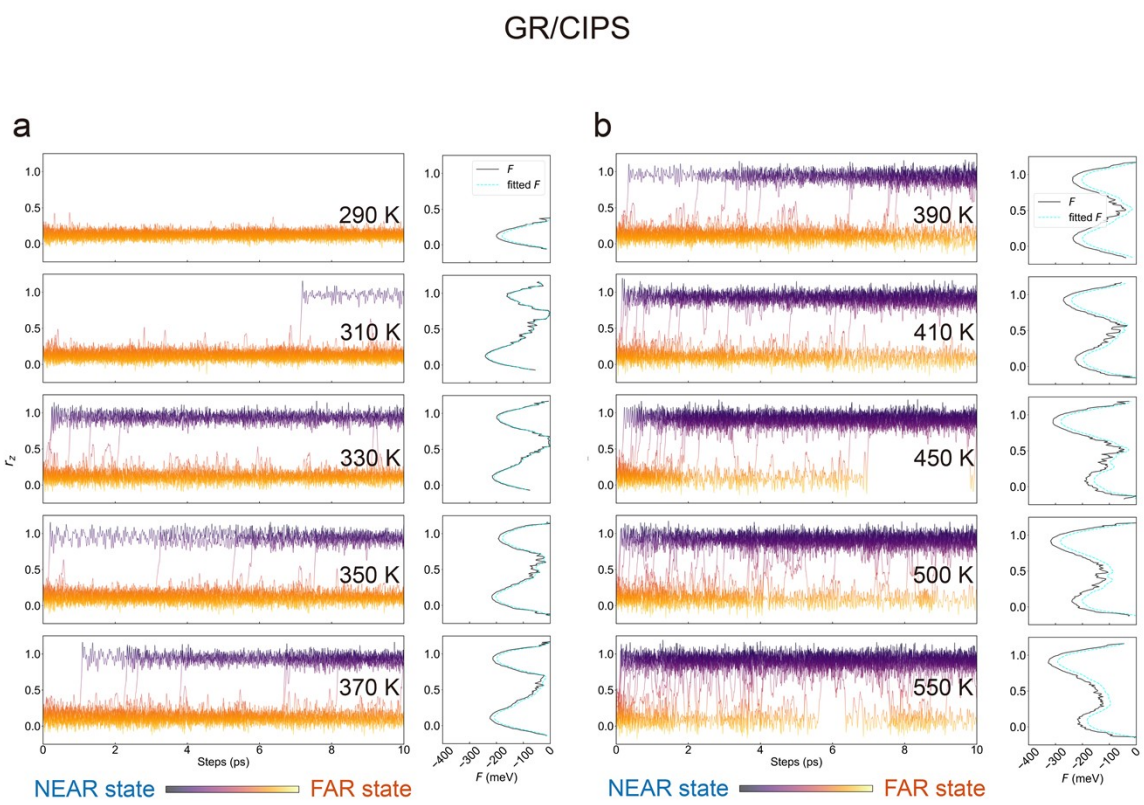

Figure S14. Temperature-dependent state switching dynamics and barriers in GR/CIPS heterostructure. The FAR state is selected as the initial state.

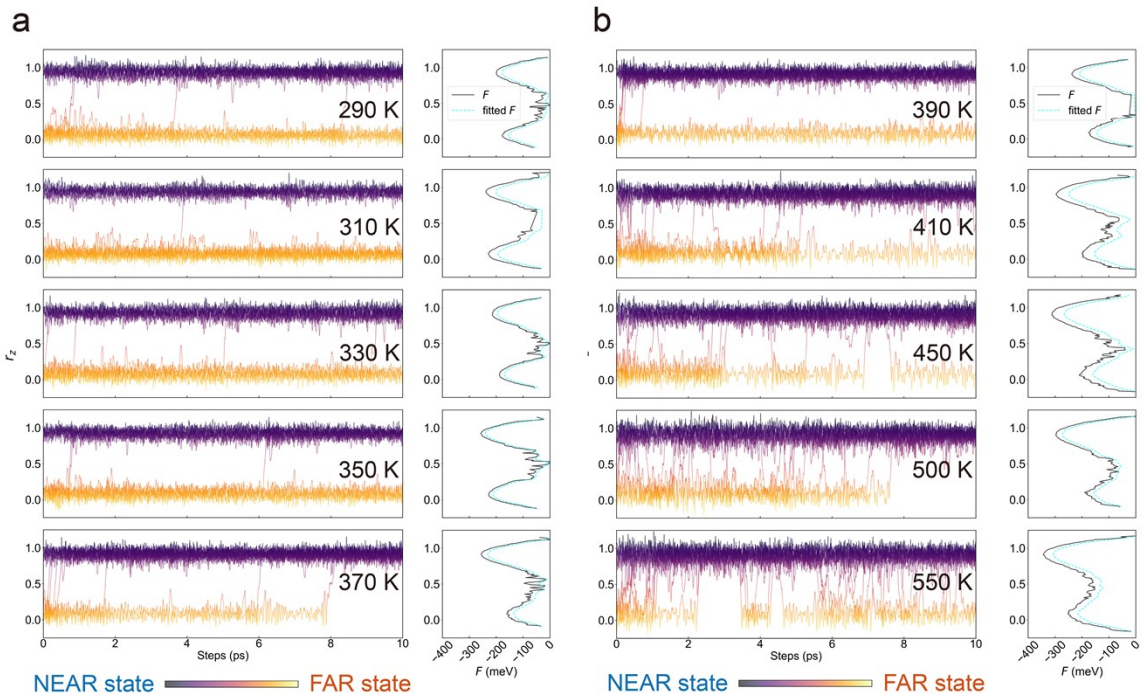

Figure S15. Temperature-dependent state switching dynamics and barriers in GR/CIPS heterostructure. The PARA state is selected as the initial state.

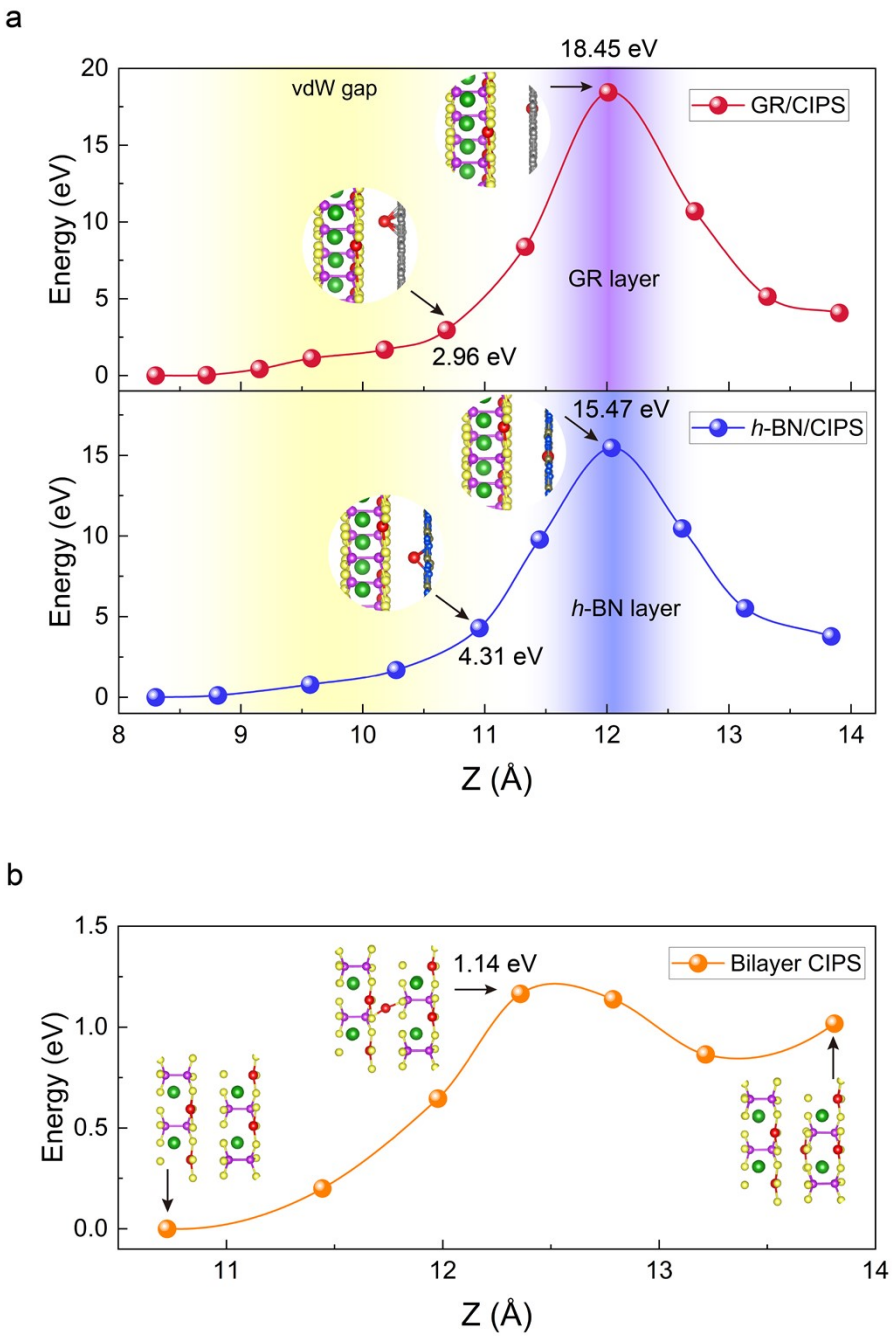

Figure S16. (**a**) Energy barriers for interlayer Cu^+ migration as a function of vertical position in CIPS-based heterostructures. The upper and lower panels corresponding to GR/CIPS and *h*-BN/CIPS, respectively. (**b**) Energy barriers for interlayer Cu^+ migration as a function of vertical position in bilayer CIPS.

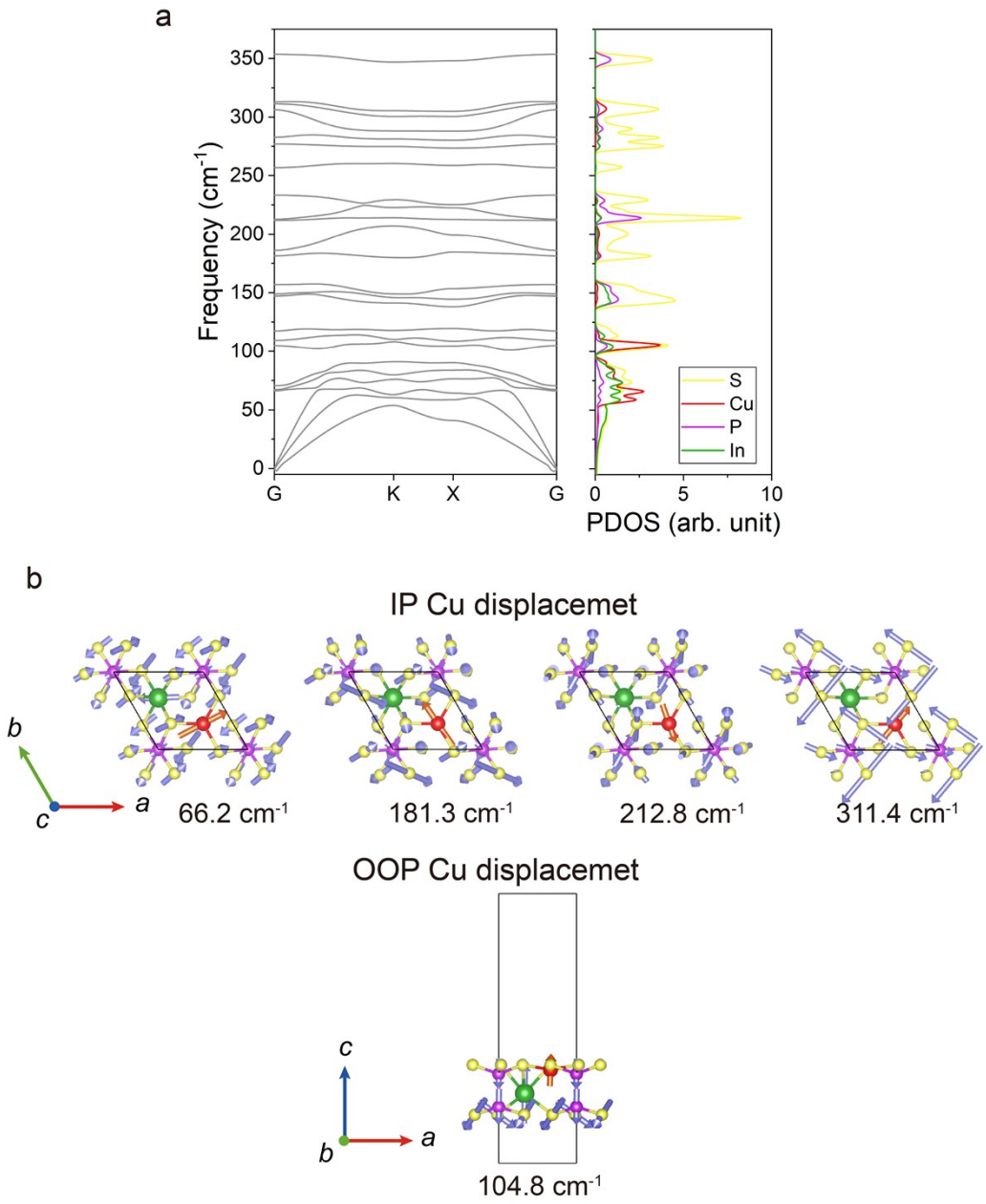

Figure S17. (**a**) Phonon dispersion and vibrational density of states in the CIPS monolayer. (**b**) Characteristic phonon vibrations of in-plane (IP) and out-of-plane (OOP) Cu displacement in the CIPS monolayer, orange vectors denote the vibration patterns of Cu atoms, while light-blue vectors correspond to all other atoms.

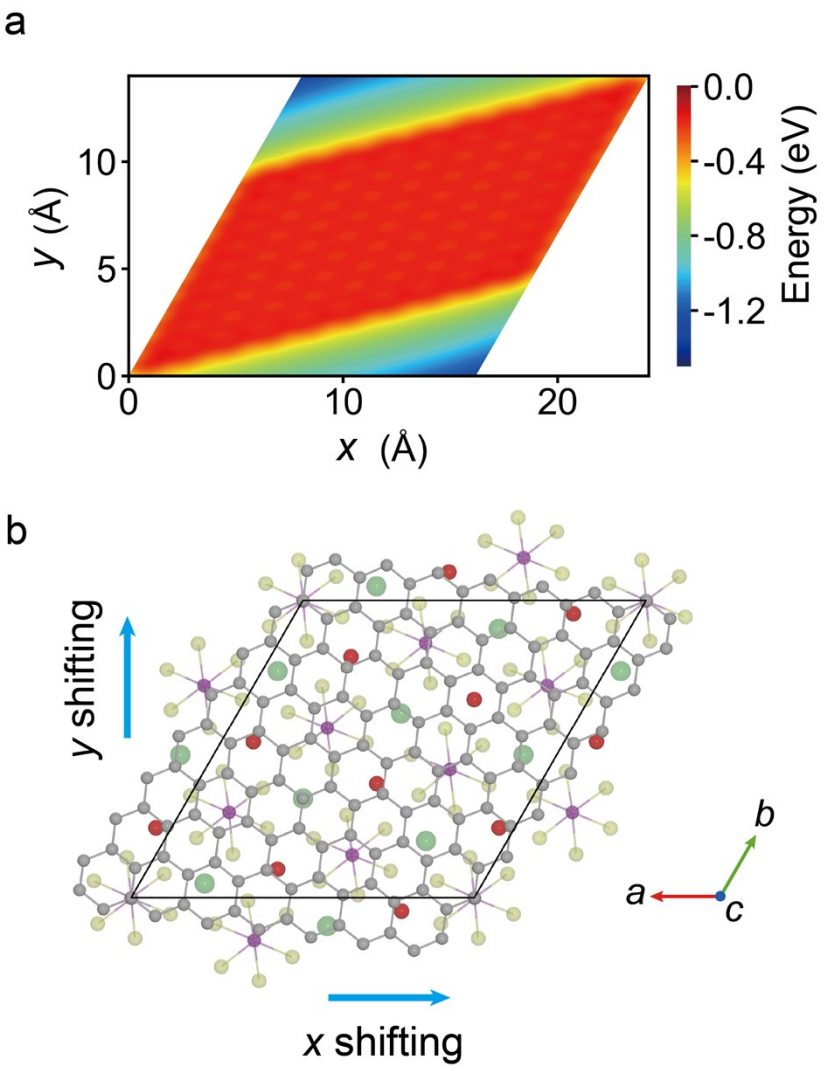

Figure S18. (**a**) Stacking energies of the GR/CIPS heterostructure. (**b**) Shifting process to generate the energy surface in (**a**), with blue arrows indicating the relative shifting directions of the CIPS layer within the *xy* plane, the color bar represents the change in total energy of the supercell.

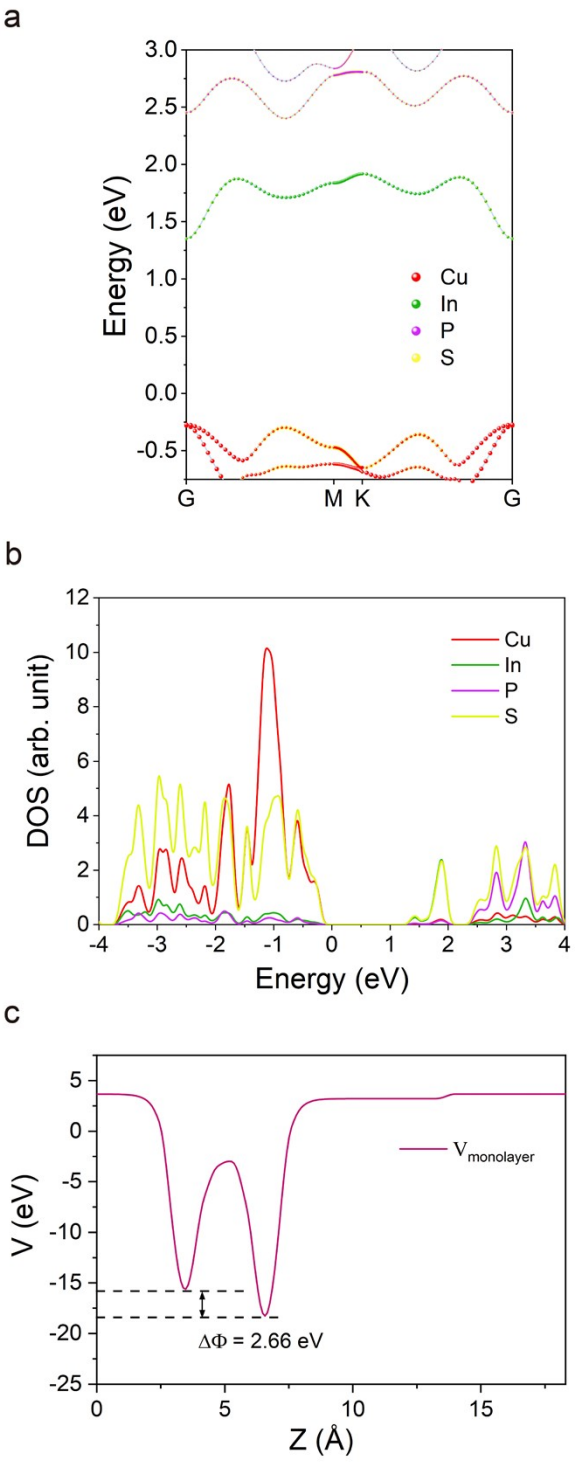

Figure S19. (**a**) Element-projected density of states (DOS), (**b**) band structure, and (**c**) electronic potential of the CIPS monolayer.

Table S1. Fitted parameters for the interlayer interactions using the LJ potential.

Heterostructure	ε (meV)	σ (Å)
h-BN/CIPS-NEAR	627.32	2.869
h-BN/CIPS-FAR	505.59	2.891
GR/CIPS-NEAR	618.28	2.906
GR/CIPS-FAR	541.06	2.909

Table S2. Structural parameters of the free-standing CIPS monolayer in NEAR and FAR states, including the polarization direction, dipole moment ($^{P_{polar}}$), and the averaged bond lengths of P-P bonds ($^{l_{P-P}}$) and S-P bonds at both sites ($^{l_{NEAR,S-P}}$ and $^{d_{FAR,S-P}}$).

Polarization state	Polarization direction	P_{polar} ($e \cdot$ Å/$u.c.$)	l_{P-P} (Å)	$l_{NEAR,S-P}$ (Å)	$l_{FAR,S-P}$ (Å)
CIPS-NEAR	↑	0.080	2.254	2.063	2.025
CIPS-FAR	↓	-0.080	2.254	2.025	2.063

note: $^{P_{polar}}$ denotes the dipole moment induced by ionic polar displacement within the CIPS layer.

Table S3. Structural deformation of passivation layers in heterostructures.

Heterostructure state	Polarization direction	P_{total} ($e \cdot$ Å$/u.c.$)	Δl (Å)
h-BN/CIPS-NEAR	↑	0.082	-0.013
h-BN/CIPS-FAR	↓	-0.045	-0.013
GR/CIPS-NEAR	↑	0.101	-0.001
GR/CIPS-FAR	↓	-0.034	-0.001

note: P_{total} indicates the total dipole moment of the entire heterostructures, including contributions from cationic polar displacement within the CIPS layer and dipole moment induced by interfacial charge transfer. Δl denotes the difference in average bond lengths of B-N and C-C bonds for the *h*-BN/CIPS and GR/CIPS heterostructures, respectively. The DFT calculated B-N and C-C bond lengths are 1.450 Å and 1.425 Å.

Table S4. Structural deformation of the CIPS layer in heterostructures, including average bond length differences of P-P bonds (Δl_{P-P}) and S-P bonds at both sides ($\Delta l_{NEAR\ side,\ S-P}$ and $\Delta l_{FAR\ side,\ S-P}$).

Heterostructure state	Polarization direction	P_{total} ($e \cdot$ Å$/u.c.$)	Δl_{P-P}(Å)	$\Delta l_{NEAR\ side,S-}$ (Å)	$\Delta l_{FAR\ side,S-P}$ (Å)
h-BN/CIPS-NEAR	↑	0.082	0.002	0.002	-0.002
h-BN/CIPS-FAR	↓	-0.045	-0.022	-0.001	0.001
GR/CIPS-NEAR	↑	0.101	-0.019	-0.003	-0.002
GR/CIPS-FAR	↓	-0.034	0.013	-0.002	-0.009

Table S5. Fitted parameters for interlayer interactions using the Buckingham potential.

Heterostructure	Δd_0 (Å)	a (meV)	b (Å^{-1})	c (meV)	C_{33} (GPa)
h-BN/CIPS-NEAR	3.52	6.70×10^6	2.428	3.57×10^6	14.3

h-BN/CIPS-FAR	3.54	5.97×10^6	2.427	3.14×10^6	10.7
GR/CIPS-NEAR	3.54	6.82×10^6	2.403	3.86×10^6	11.3
GR/CIPS-FAR	3.58	5.97×10^6	2.390	3.49×10^6	10.4

Table S6. Schottky barrier heights of the GR/CIPS heterostructure.

Heterostructure	Φ_n (eV)	Φ_p (eV)	contact type
GR/CIPS-NEAR	0.27	1.34	*n*-type
GR/CIPS-PARA	0.15	1.51	*n*-type
GR/CIPS-FAR	0.05	1.58	quasi-Ohmic

Table S7. Tunneling barrier width (w_{TB}), tunneling height (Φ_{TB}), and tunneling probability (P_{TB}) of carriers across *h*-BN/CIPS and GR/CIPS in the NEAR and FAR states.

Heterostructure	w_{TB} (Å)	Φ_{TB} (eV)	P_{TB}(%)
h-BN/CIPS-NEAR	2.13	5.67	0.55
h-BN/CIPS-FAR	2.12	5.95	0.50

GR/CIPS-NEAR	2.13	5.69	0.55
GR/CIPS-FAR	2.08	5.95	0.55

Table S8. Fitted barrier height of Cu switching (ΔF) in the CIPS monolayer and *h*-BN/CIPS and GR/CIPS heterostructures at different temperatures.

Temperature (K)	ΔF_{CIPS} (meV)	$\Delta F_{h-BN/CIPS}$ (meV)	$\Delta F_{GR/CIPS}$ (meV)
290	201.4	155.5	199.2
310	209.0	185.2	191.7
330	257.3	204.0	214.5
350	220.1	205.7	257.1
370	210.1	229.5	243.5
390	185.7	185.7	237.6
410	183.1	176.2	234.6
450	169.7	160.7	219.9
500	167.0	149.2	204.7
550	142.4	145.7	192.6

note: ΔF values are extracted by setting the NEAR state as initial state.

Table S9. Lattice constants of unit cells in free-standing monolayers.

Monolayer	Lattice constant (Å)
h-BN	2.512
GR	2.468
CIPS-FE	6.124

Table S10. Lattice constants and lattice mismatch (δ) of heterostructures.

Heterostructure	Lattice constant (Å)	δ (%)
h-BN/CIPS	16.312	1.75
GR/CIPS	16.168	0.02

Table S11. Electrostatic potential of vacuum regions in *h*-BN/CIPS and GR/CIPS heterostructures.

Heterostructure	$V_{vacuum,passivation\ side}$	$V_{vacuum,\ CIPS\ side}$	ΔV
h-BN/CIPS-NEAR	3.264	2.811	0.45

h-BN/CIPS-PARA	3.057	2.931	0.13
h-BN/CIPS-FAR	2.840	3.085	0.25
GR/CIPS-NEAR	3.442	2.878	0.56
GR/CIPS-PARA	3.222	3.025	0.20
GR/CIPS-FAR	2.992	3.183	0.19

note: $V_{vacuum,\ passivation\ side}$ denotes the $V_{vacuum,\ h-BN\ side}$ and $V_{vacuum,\ GR\ side}$ for the *h*-BN/CIPS and GR/CIPS heterostructures, respectively. ΔV is determined as $\Delta V = |V_{vacuum,\ passivation\ side} - V_{vacuum,\ CIPS\ side}|$.

Section I. Methods of first-principles simulations

First-principles calculations are performed relying on density functional theory (DFT) within the projector augmented wave (PAW) formalism as implemented in the Vienna *ab initio* Simulation Package (VASP).[1] The Perdew-Burke-Ernzerh of generalized gradient approximation is used to describe the exchange-correlation interactions,[2] while the Grimme-D3 method is adopted for the interatomic vdW interactions.[3] The wavefunctions are expanded on a plane-wave basis set employing a cutoff energy of 500 eV. The Brillouin zone is sampled using a $4 \times 4 \times 1$ k-point mesh. All the structures are relaxed until the total energy converges to within 10^{-5} eV and the Hellman-Feynman force on each atom is less than 0.01 eV/Å. For the

2D thin film model, the slabs from neighboring cells are separated by a vacuum layer of 20 Å to avoid spurious interactions. Furthermore, a dipole correction is applied along the z direction. The polarization values are calculated by directly integrating the product of charge density and atomic position without adopting the Berry phase method.[4] The climb image-nudge elastic band (CI-NEB) method is applied to compute the energy migration pathway for Cu^+ interlayer moving. Most of the data post-processing is performed using the VASPKIT plugin.[5] The atomic structure views are obtained through the VESTA software.[6]

The interface Schottky barrier heights (SHBs) are defined and calculated as $\Phi_n = E_{CBM} - E_{Fermi}$ for electrons and $\Phi_p = E_{Fermi} - E_{VBM}$ for holes, according to the Schottky-Mott model,[7] where E_{CBM} and E_{VBM} are the CBM and VBM of CIPS layer, and E_{Fermi} is the Fermi level of the heterostructure. An Ohmic contact forms when Φ_n or Φ_p approaches zero; otherwise, a Schottky contact exists.

To quantitatively determine the free-energy barrier of Cu^+ switching, molecular dynamics (MD) simulations are performed for both the freestanding CIPS monolayer and the heterostructures across temperatures ranging from 290 K to 550 K in increment of 20 K. The MD simulations are performed using the machine leaning force field (MLFF) approach implemented in VASP. The MLFF is trained using Gaussian process regression with Bayesian error estimation, relying on a "on-the-fly" process for the selection of training structures. The MD simulations adopt an isothermal–isochoric (NVT) ensemble relying on a Nosé–Hoover thermostat.

The production runs are performed in larger $\sqrt{3} \times 1 \times 1$ supercells based on the constructed heterostructures in **Figure 1d, e**. For each temperature, a 10 ps MD is carried out with a timestep of 1 fs. The final 5 ps of equilibrated trajectories are used to drive r_Z.

In the MD simulations, the temperature-dependent vibrational density of states ($VDOS$) are calculated as: [8, 9]

$$VDOS(\omega) = \int_0^{t_{max}} e^{-i\omega t} C_v(t) dt \tag{1}$$

$$C_v(t) = \sum_{i=1}^{N} \frac{\langle v_i(0) v_i(t) \rangle}{\langle v_i(0)^2 \rangle} \tag{2}$$

where $C_v(t)$ is the normalized auto-correlation function of atomic velocity, subscript i represents the i-th Cu atom among *N* Cu atoms, and $v(t)$ is the atomic velocity at time t.

Section II. Simulation models

The optimized lattice constants of these monolayers are listed in **Table S9**, showing good agreement with experimental results.[10-12] Additionally, appropriate supercells and isotropic lattice mismatching for monolayer stacking are considered to eliminate unphysical internal stress and enhance structure stability. The hexagonal $\sqrt{43} \times \sqrt{43} \times 1$ slab of the passivation layer (*h*-BN or GR monolayer) is

constructed to match the $\sqrt{7} \times \sqrt{7} \times 1$ slab of CIPS. The lattice mismatch (δ) is 1.75% for *h*-BN/CIPS and 0.02% for GR/CIPS (**Table S10**). The lowest-energy stacking configuration is determined by shifting the *h*-BN or GR layer relative to the CIPS layer within the whole *xy* plane, and the lowest-energy structures are shown in **Figure 1**, with the corresponding 2D energy surface presented in **Figure S18**.

Section III. Polarization switching acting on structure and electronic properties

For the *h*-BN/CIPS heterostructure, *h*-BN exhibits slight B-N bond deformation in both polarization states, whereas the CIPS layer undergoes pronounced vertical compression with shortened P-P bond length (decrease of ~ 0.022 Å, see **Table S4**) in the FAR state, while negligible deformation in the NEAR state (increase of ~ 0.002 Å, see **Table S4**). For the GR/CIPS interface, the CIPS layer experiences compression-stretching deformation with distorted S-P bonds upon switching from the NEAR state to the FAR state, induced by the concerted switching of Cu^+ ions, while the GR layer remains rigid with negligible changes. This is consistent with the larger bending moduli of the GR monolayer compared to *h*-BN and CIPS.[13-15] Recent experiments and theoretical calculations on bulk-phase CIPS also reveal its much smaller Young's moduli compared with *h*-BN and GR.[16-20] Therefore, *h*-BN and GR are appropriate capping layers to mechanically protect the inner, relatively "softer" CIPS layer.

An examining of the electronic properties of 2D vdW monolayers helps in understanding the more complicated scenarios in heterostructures. The GR monolayer is a zero-gap semiconductor with a Dirac cone, composed of the lowest conduction band (CBM) of carbon π^* orbital and highest valence band (VBM) of carbon π orbital, with the Fermi level located at the K point. Its semi-metallic characteristic is relatively sensitive to external stress and impurities.[21-23] In contrast, the *h*-BN monolayer is an insulator with a wide direct gap located at the K point. For FE CIPS, the monolayer exhibits a band gap of 1.62 eV at the Γ point (**Figure S19a, b**). The CBM primary originates from In and S atomic states with minor contributions from Cu and P, while its VBM stems from hybridized states of Cu and S. The intrinsic dipole of FE CIPS is 0.080 $e \cdot \text{Å}$ per unit cell.

Band alignment diagrams are constructed from calculated vacuum energy references and FE-dependent work functions, providing a quantitative description of the interfacial electronic structure. This model corresponds to the idea vdW-contact limit. Extrinsic inhomogeneities, such as induced by trapped hydrocarbons or fabrication-induced disorder, may reduce spatial uniformity but do not affect the underlying ferroionic-governed configuration mechanism.

The projected band structure and density of states (DOS) of these two heterostructures in both the NEAR and FAR states are shown in **Figure S5**. In the NEAR state, *h*-BN/CIPS exhibits a direct band gap (1.57 eV) at the Γ point, with dominant VBM and CBM states originating from CIPS. In contrast, at the FAR

state, an indirect band gap emerges due to a relative upward shift of the valance band of *h*-BN, reducing the band gap to 1.24 eV (**Figure S5a, b**). Thus, polarization reversal significantly influences the electronic structure of *h*-BN/CIPS. For the GR/CIPS heterostructure, the Dirac cone of GR is preserved (**Figure S5c, d**). In the NEAR state, there is an apparent lift of band degeneracy at the M point, composed of π orbitals of GR. Interestingly, upon switching the contacting CIPS into the FAR state, the Dirac cone shifts above the Fermi level (**Figure S5d**), implying *p*-type doping in GR at the FAR state.

The variation in E_{eff} induces different interfacial electrostatic potential drops (ΔV) between the two sides of the heterostructures. For *h*-BN/CIPS, $\Delta V = |V_{vacuum,\ h-BN\ side} - V_{vacuum,\ CIPS\ side}|$, determined as the difference between the electrostatic potentials on the *h*-BN ($V_{vacuum,\ h-BN\ side}$) and CIPS ($V_{vacuum,\ CIPS\ side}$) sides, decreases from 0.45 eV in the NEAR state to 0.24 eV in the FAR state. Similarly, for GR/CIPS, ΔV reduces from 0.56 eV in the NEAR state to 0.19 eV in the FAR state (also see **Figure S7** and **Table S11**).

References:

1. G. Kresse and J. Furthmüller, Comp Mater Sci, 1996, 6, 15-50.
2. J. P. Perdew, K. Burke and M. Ernzerhof, Phys. Rev. Lett., 1996, 77, 3865.
3. S. Grimme, S. Ehrlich and L. Goerigk, J. Comput. Chem., 2011, 32, 1456-1465.
4. H. Wang and X. Qian, npj Comput. Mater., 2019, 5, 119.

5. V. Wang, N. Xu, J.-C. Liu, G. Tang and W.-T. Geng, Comput. Phys. Commun., 2021, 267, 108033.
6. K. Momma and F. Izumi, J. Appl. Crystallogr., 2008, 41, 653-658.
7. T. V. Vu, A. I. Kartamyshev, T. H. Ho, N. N. Hieu, H. V. Phuc, S.-T. Nguyen and C. V. Nguyen, Langmuir., 2024, 40, 20783-20790.
8. Y. Yu, C. Yang, M. Baggioli, A. E. Phillips, A. Zaccone, L. Zhang, R. Kajimoto, M. Nakamura, D. Yu and L. Hong, Nat. Commun., 2022, 13, 3649.
9. I. Noda, Appl. Spectrosc., 1993, 47, 1329-1336.
10. V. Solozhenko, G. Will and F. Elf, Solid State Commun., 1995, 96, 1-3.
11. J. Wintterlin and M.-L. Bocquet, Surf. Sci., 2009, 603, 1841-1852.
12. V. Maisonneuve, M. Evain, C. Payen, V. Cajipe and P. Molinie, J. Alloys Compd., 1995, 218, 157-164.
13. Q. Lu, M. Arroyo and R. Huang, J. Phys. D: Appl. Phys., 2009, 42, 102002.
14. J. Wu, B. Wang, Y. Wei, R. Yang and M. Dresselhaus, Mater. Res. Lett., 2013, 1, 200-206.
15. B.-C. Tran Khac, F. W. DelRio and K.-H. Chung, ACS Appl. Mater. Interfaces., 2018, 10, 9164-9177.
16. K. Bu, T. Fu, Z. Du, X. Feng, D. Wang, Z. Li, S. Guo, Z. Sun, H. Luo and G. Liu, Chem. Mater., 2022, 35, 242-250.
17. X. Jiang, X. Zhang, R. Niu, Q. Ren, X. Chen, G. Du, Y. Chen, X. Wang, G. Tang and J. Lu, Adv. Funct. Mater., 2023, 33, 2213561.

18. M. Shao, Y. Yang, R. He, R. Zhao, X. Renshaw Wang, Z. Zhong, H. Liu, Y. Yang and T. L. Ren, Adv. Electron. Mater., 2023, 9, 2300352.
19. T. Herden, M. Ternes and K. Kern, Nano Lett., 2014, 14, 3623-3627.
20. J.-U. Lee, D. Yoon and H. Cheong, Nano Lett., 2012, 12, 4444-4448.
21. S. Y. Zhou, G.-H. Gweon, A. Fedorov, P. First, de, W. De Heer, D.-H. Lee, F. Guinea, A. Castro Neto and A. Lanzara, Nat. Mater., 2007, 6, 770-775.
22. S. Zhou, D. Siegel, A. Fedorov, F. E. Gabaly, A. Schmid, A. C. Neto, D.-H. Lee and A. Lanzara, Nat. Mater., 2008, 7, 259-260.
23. A. J. Samuels and J. D. Carey, ACS Nano., 2013, 7, 2790-2799.